

# Surface wrinkling of plasma-exposed PDMS is caused by water vapour sorption: an optical environmental sensor

Zain Ahmad,<sup>a</sup> Gunjan Tyagi,<sup>a</sup> Shuning Xiang,<sup>a</sup> Jerry Heng,<sup>a</sup> Pedro Patrício,<sup>b,c</sup> Paulo I. C. Teixeira,<sup>b,c</sup> Christopher M. Stafford,<sup>d</sup> Jack F. Douglas,<sup>d</sup> João T. Cabral<sup>a\*</sup>

Wrinkling of polydimethylsiloxane (PDMS) has unlocked a plethora of technological applications, from tuneable surface wetting to photonic response. Surface undulations with prescribed wavelength and amplitude are excited by in-plane mechanical compression of bilayers comprising a thin, stiff outer skin on a soft elastomer or gel. Plasma oxidation has become ubiquitous for creating such thin ( $\approx 10$  nm) glassy interfacial layers. Spontaneous wrinkling can occur even in the absence of external mechanical strain fields, which has been rationalised in terms of a thermally-induced strain that accompanies the expansion-contraction cycle of such laminate films. Here, we show that exposure to water vapour is, instead, responsible for surface wrinkling, due to the swelling the oxidised skin layer. This interpretation of surface wrinkling provides a rationale for the apparent experimental variability of the wrinkling process. We verify this hypothesis experimentally by observing and modelling the spatiotemporal evolution of the reversible wrinkling process under a range of controlled environmental conditions. From a practical standpoint, we find that this effect provides for a facile approach for humidity sensing, through structural colour changes arising from the diffractive wrinkled skin.

Keywords: wrinkling, PDMS, plasma, relative humidity, sensor, structural colour, reversible

## 1 Introduction

Soft lithography,<sup>1</sup> a suite of non-photolithographic approaches to fabricate nano- and microstructures, has transformed the ability to surface pattern at low cost and without resorting to specialist equipment or materials. In particular, surface wrinkling and buckling have emerged as powerful means to generate periodic topographies, from a few 10s nm to 100s  $\mu\text{m}$ , over large areas,<sup>2</sup> harnessing a mechanical instability of a sandwich bilayer.<sup>3-5</sup> The in-plane compression of a thin, stiff film, attached to a soft substrate often gives rise to highly regular, periodic undulations, with prescribed wavelength, amplitude and in-plane morphology,<sup>6</sup> over large areas. The skin layer can be fabricated by depositing a stiff material, via lamination, spin coating, sputtering, or evaporation, or by surface chemical modification or reaction.<sup>2,7-10</sup>

Polydimethylsiloxane (PDMS) elastomers are ubiquitously employed as the substrate, due to a combination of physical-chemical properties, from optical transparency and incompressibility, to surface chemistry and tunable adhesion and wettability.<sup>11,12</sup> Surface oxidation of PDMS, via plasma, ultraviolet or UV-ozone exposure, is commonly employed to generate the

high modulus ( $\approx \text{GPa}$ ) glassy  $\text{SiO}_x$  skin layer, well-bonded to the substrate (thus robust to delamination), whose thickness ranges from  $\approx 10$  nm (plasma) to  $\approx 1 \mu\text{m}$  (UVO).<sup>13-15</sup> Oxidation cleaves  $\text{Si-CH}_3$  groups, which are progressively replaced by hydroxyl groups and oxide links leading to a directional densification front<sup>16,17</sup> of the silica-like skin layer, providing the large mechanical contrast between skin and substrate modulus required for wrinkling. In the 1990s, Whitesides and co-workers first reported on the regular patterning via surface wrinkling of PDMS bilayers formed by metal evaporation,<sup>8</sup> or plasma oxidation,<sup>18</sup> rationalised in terms of the thermal excursion experienced during deposition: “the PDMS is heated, and its surface oxidized (...) when the PDMS cools, it contracts and places the silicate layer under compressive stress”<sup>18</sup> which is relieved by the emergence of highly ordered surface undulations, and widely followed since.<sup>19-21</sup> On planar PDMS surfaces, sinusoidal wrinkling patterns are isotropic with well-defined wavelength and amplitude, but pattern symmetry can be broken with multi-level or imprinted topographies, or via external mechanical fields, that lead to strikingly complex and functional patterns.

Our paper starts from the initially puzzling observation (Fig. 1a) that, when plasma-oxidised PDMS films are subsequently placed under an inert atmosphere (such as argon), no wrinkling patterns are observed. By contrast, when placed in atmospheric conditions, the widely observed wrinkling behaviour is recovered. However, the wrinkling amplitude is found to slowly evolve with time, on timescales of minutes to days, depending on environmental conditions. Taken together, these observations appear contrary to the traditional thermal cycling hypothesis. We replace

<sup>a</sup> Department of Chemical Engineering, Imperial College London, London SW7 2AZ, UK

<sup>b</sup> Departamento de Física, ISEL - Instituto Superior de Engenharia de Lisboa, Instituto Politécnico de Lisboa, 1959-007 Lisboa, Portugal

<sup>c</sup> Centro de Física Teórica e Computacional, Faculdade de Ciências, Universidade de Lisboa, 1749-016 Lisboa, Portugal

<sup>d</sup> Materials Science and Engineering Division, National Institute of Standards and Technology, Gaithersburg, MD, USA

\* Corresponding author. Email: j.cabral@imperial.ac.uk

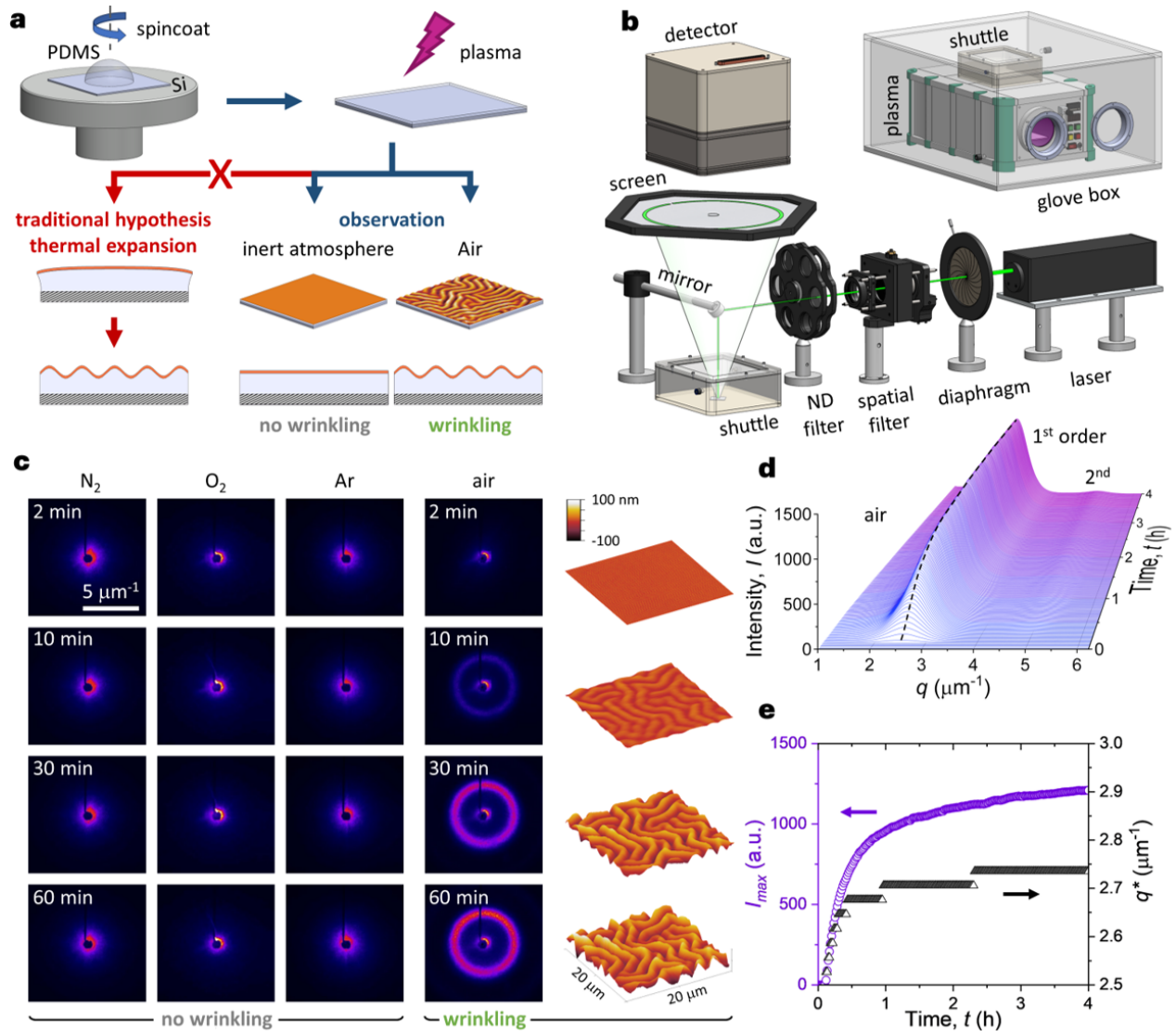


**Figure 1** Trigger and spatio-temporal evolution of oxidised PDMS wrinkling. **a**, Schematic of the spontaneous isotropic wrinkling in oxidised PDMS films in air vs. in inert atmosphere, contrasting with the established thermal cycling mechanism. **b**, Experimental setup employed for plasma exposure and small-angle light scattering (SALS) in controlled atmosphere, employing a custom-built glove box and shuttle; SALS probes the laser light surface diffraction in reflection mode, quantifying pattern wavelength  $\lambda$  and amplitude  $A$ . **c**, Representative diffraction patterns of plasma oxidised PDMS ( $P=99$  W,  $t_p=5$  min,  $p=0.2$  mbar,  $H=11$   $\mu\text{m}$ ) surfaces exposed to  $\text{N}_2$ ,  $\text{O}_2$ , Ar, and air, at intervals of 2, 10, 30 and 60 min following plasma exposure; corresponding AFM images of the oxidised PDMS sample in air. **d**, Evolution of the radially averaged scattering intensity of the oxidised PDMS film. **e**, Intensity of the 1<sup>st</sup> diffraction order ( $I_{\text{max}}$ ,  $\circ$ ) and corresponding wavenumbers ( $q^*$ ,  $\triangle$ ) as a function of time.

this hypothesis by elucidating the differential sorption of the bi-layer structure and introduce a model that can quantitatively account for all previous observations, and exploit the environmental susceptibility of PDMS surface wrinkling in an optical sensor.

## 2 Results and Discussion

### 2.1 Oxidised PDMS response under controlled atmosphere

PDMS films with varying thickness ( $H$ ), from 100 nm to 100s  $\mu\text{m}$ , were customarily obtained by spin-coating on silicon wafers and thermally cross-linked.  $\text{O}_2$  plasma exposure of these films, results in bilayer structures with a thin glassy-like surface layer of thickness  $h$  (depending on plasma power, pressure, and exposure time), on top of the bulk PDMS. In our experiments, the plasma

generator was housed inside a custom built glove box and, following oxidation, the films were kept under controlled environmental conditions, and transported for analysis by small angle light scattering (SALS) and atomic force microscopy, using an environmental ‘shuttle’, illustrated in Fig. 1b and SI section S1. Following plasma exposure (power  $P=99$  W, exposure time  $t_p=5$  min, and  $\text{O}_2$  pressure  $p=0.2$  mbar), the PDMS films did not exhibit wrinkling when the shuttle contained  $\text{N}_2$ ,  $\text{O}_2$ , or Ar, but readily undulated when exposed to air, as shown in Fig. 1c. Its surface topography was also monitored over time with AFM (shown at  $t=2, 10, 30$  and  $60$  min from exposure to air), revealing an increase in amplitude of the pattern. Figure 1d shows the evolution of the radially averaged SALS intensity over time. The dashed line in-

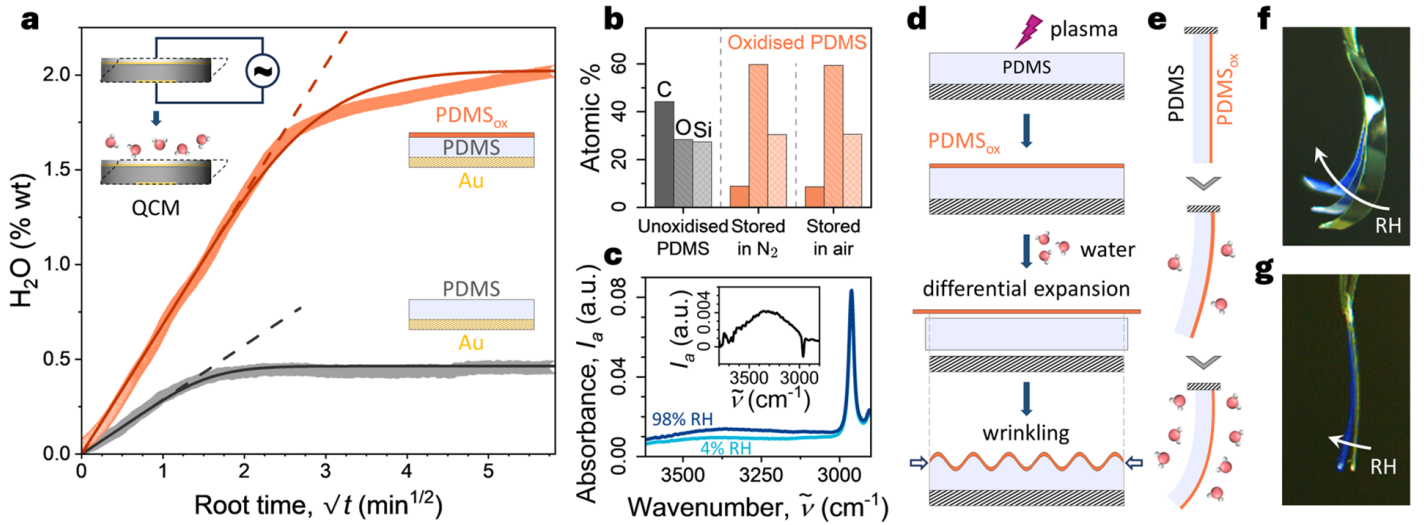


**Figure 2** Humidity induces wrinkling. **a**, Difference in water sorption between neat and oxidised (99 W, 5 min, 0.2 mbar) thin PDMS films ( $H \approx 100$  nm), spin-coated on Au sensor, quantified in terms of water content measured by QCM following an RH jump from 11 to 97%. Solid lines are fits to a diffusion into plane sheet model, and dashed lines correspond to the short time diffusion approximation (see text). **b**, Atomic elemental composition of the surface of neat and oxidised PDMS, subsequently stored in  $N_2$  and air ( $\approx 50\%$  RH for  $\approx 3$  h), obtained by XPS (at low pressure  $<10^{-7}$  Pa). **c**, FTIR spectra of plasma-oxidised PDMS stored in 98% and 4% RH environment, showing the presence of a water O-H stretching band (evidenced by the difference of spectra, shown in inset). **d**, Schematic of spontaneous wrinkling of plasma-oxidised PDMS due to differential swelling of the skin and bulk PDMS in the presence of water vapour. **e**, Illustration of a hanging PDMS asymmetric beam plasma oxidised on one side and exposed to increasing humidity, clamped vertically by one extremity. **f-g**, Composite motion optical images showing how plasma-oxidized PDMS beams of different thicknesses bend when exposed to increasing relative humidity (from 6% to 85% RH). The beam in **f**, measures 12 mm  $\times$  2 mm with a thickness  $H \approx 53$   $\mu$ m, while the beam in **g**, is 11 mm  $\times$  1.5 mm with a thickness  $H \approx 138$   $\mu$ m. For clarity, the later positions of the beams have been highlighted in blue.

indicates the first diffraction order, while the second order appears at later times. A progressive increase in peak intensity  $I_{max}$  of the isotropic diffraction pattern was observed, while the position of the intensity maximum  $q^*$  remained largely constant (Fig. 1e), corresponding to a wrinkling wavelength  $\lambda \approx 2.3$   $\mu$ m (decreasing by  $\approx 10\%$ , over several hours). Controlled thermal cycling experiments of plasma oxidised PDMS film in an inert atmosphere confirmed that wrinkles do not emerge in inert atmosphere (SI section S2). Instead of the widely-accepted thermal excursion mechanism, our results suggest that water sorption is responsible for surface wrinkling, and we therefore set out to investigate the effect of humidity on the emergence of wrinkling.

We note that Breid and Crosby<sup>22</sup> have previously found that ethanol vapor would preferentially swell the oxidised PDMS skin, compared to bulk PDMS, resulting in surface wrinkling, and swelling of silica glassy layers by water, associated with the formation of silanol group has been well documented.<sup>23</sup>

## 2.2 Quantifying differential water sorption

In order to elucidate the cause of interfacial stress in the oxidised PDMS bilayer, we employ a quartz crystal microbalance (QCM), widely used to gravimetrically investigate sorption in ultra-thin layers,<sup>24</sup> to examine the differential swelling of the glassy skin layer and underlying PDMS film in a humid environment (SI section S3). PDMS films of  $H \approx 100$  nm were spincoated on Au sensors and thermally cured. One film was exposed to  $O_2$  plasma for 5 min (99 W, 0.2 mbar) resulting in an oxide ( $SiO_x$ ) skin layer of thickness,  $h \approx 20$  nm.<sup>16,17,25</sup> Unoxidised and oxidised films were then subjected to an RH jump from  $\approx 11$  to 97% and the mass

change recorded over time (Fig. 2a). PDMS is found to uptake  $\approx 0.5\%$  mass fraction of water (in line with  $\approx 0.7\%$  found<sup>26</sup> by dynamic vapour sorption, DVS). By contrast, the water sorbed by oxidised PDMS films exceeds 2%, which corresponds to  $\approx 8\%$  for the oxidised skin layer alone.

The mass uptake at short times follows the  $t^{1/2}$  dependence appropriate for Fickian diffusion (dashed lines in Fig. 2a). Assuming 1D diffusion into a plane sheet with a no-flux boundary condition at the opposite face, the mass sorbed at time  $t$  in this simple model equals,<sup>27</sup>

$$\frac{M_t}{M_\infty} = 1 - \sum_{n=0}^{\infty} \frac{8}{(2n+1)^2 \pi^2} \exp\left(-D_{\text{eff}}(2n+1)^2 \pi^2 \frac{t}{4l^2}\right) \quad (1)$$

where  $M_\infty$  is the equilibrium mass,  $l$  is the sheet thickness, and  $D_{\text{eff}}$  is an effective diffusion coefficient, which can be approximated to  $M_t/M_\infty = (2/l)\sqrt{(D_{\text{eff}} t)/\pi}$  at short times (SI section S4).<sup>24,28</sup> We obtain  $D_{\text{eff}} \approx 6 \times 10^{-15}$   $\text{cm}^2/\text{s}$  for oxidised PDMS and  $5 \times 10^{-13}$   $\text{cm}^2/\text{s}$  for unoxidised PDMS, thus indicating that the water vapour diffuses much slower in the densified, glassy oxide layer than in PDMS (this is in line with the suppressed oxygen diffusion observed<sup>29</sup> in oxidised PDMS, and of water in silica glass<sup>30</sup>). We note that sorption kinetics can be more complex in glassy polymer materials (e.g., type II diffusion<sup>31</sup>) but this effect is presumably not prevalent in the present system because of the nanoscale thickness of the skin layer.

Our measurements show that, while water vapour diffusion kinetics within the glassy, oxidised PDMS film ( $SiO_x$ ) is much slower than that of pure PDMS, the extent of swelling is greater than that of neat PDMS. Plasma exposure has thus a distinct effect on

the swelling and on the molecular dynamics of the glassy skin layer of the PDMS elastomer, imparting greater affinity to moisture (and this yielding a larger expansion which results in surface wrinkling), while introducing polar groups and charged groups which alter the cohesive energy density of network, leading to sluggish molecular dynamics in the oxidised layer and thus slower diffusion processes, which control wrinkling kinetics and equilibration.

To determine whether water vapour sorption chemically modifies the oxide layer, X-ray photoelectron spectroscopy (XPS) analysis was carried out in neat and oxidised PDMS, following storage in  $N_2$  and air, then measured at low pressure,  $p < 10^{-7}$  Pa (SI section S5). As expected, the elemental surface composition of PDMS changes upon oxidation, but no irreversible changes were found upon water sorption (Fig. 2b). FTIR spectroscopy of oxidised films placed at two different humidities, 98% and 4% RH, confirms the presence of water at high RH, indicated by the O-H stretching band around  $3400 \text{ cm}^{-1}$  (Fig. 2c and SI section S6). The proposed mechanism responsible for wrinkling was thus confirmed to be the differential swelling of the glassy skin caused by water sorption, as illustrated in Fig. 2d. We further corroborate our interpretation with a bilayer beam bending experiment at varying RH (Fig. 2e-g, SI video 1, SI section S7): beams of PDMS with thicknesses  $H \approx 53 \text{ }\mu\text{m}$  and  $138 \text{ }\mu\text{m}$  were exposed to plasma on one side to create a glassy skin. Within a glove box at low RH, one extremity of the beam was fixed and a gradual increase in humidity was found to result in beam deflection, as expected for the excess swelling of the oxidised layer, as shown by optical images and illustrated in the schematic. The maximum deflection of the beam decreases with the increase in the thickness of the PDMS film thickness, owing to the increase in the bending stiffness. A preferential swelling of the oxide layer with ethanol vapor (and other selective solvents) has been previously reported on UVO-oxidised PDMS, and a series of morphological transitions observed, from hexagonally-packed dimples to herringbone and labyrinthic patterns,<sup>20,22,32,33</sup> analogous to the ‘isotropic’ surface morphologies reported here.

### 2.3 Wrinkling pattern evolution during sorption

SALS experiments were employed to quantify the effect of humidity on the emergence and spatio-temporal evolution of wrinkling patterns. Fig. 3a shows the intensity of the 1<sup>st</sup> diffraction order of a representative PDMS film surface ( $H=11 \text{ }\mu\text{m}$ ,  $P=99 \text{ W}$ ,  $t_p=5 \text{ min}$ , and  $O_2$  pressure  $p=0.2 \text{ mbar}$ ) at five illustrative RH. AFM scans (Fig. 3b) were performed after 20 h, when the topography approaches an RH-dependent asymptote. The diffraction intensity is not detectable until a characteristic onset time,  $t_c$ , which is also RH-dependent. A characteristic time for wrinkling, estimated at 90% of the peak SALS intensity value,  $\tau_{90\%}$ , ranges from  $\approx 0.2 \text{ h}$  to  $18 \text{ h}$  for RH values of 98% and 22%, respectively (Fig. 3c). The wrinkling amplitude, measured at the conclusion of the experiment, appears to scale linearly with RH and is plotted in Fig. 3c, while the wrinkling wavelength,  $\lambda \approx 2.1 \text{ }\mu\text{m}$ , remained largely constant. No light diffraction or topography was observed  $\leq 6\%$  RH for two weeks, an effect that we interpret be-

low as being associated with the threshold humidity required for the swelling-induced stress to exceed the critical value for surface wrinkling. Upon exposing oxidised films to ambient conditions, wrinkles form within timescales of min to h depending on RH, and  $\leq 1 \text{ min}$  upon direct immersion in deionised (DI) water (SI section S8-9).

The growth kinetics of the amplitude of the isotropic wrinkling patterns can be estimated from the SALS analysis of a surface phase grating<sup>34,35</sup> (or the emergence of structural colour<sup>36,37</sup>) as,

$$I \approx \sum_{p=-\infty}^{\infty} J_p^2 \left( \frac{2\pi A}{\Lambda[n-1]} \right) \text{sinc}^2 \left[ \frac{W}{\pi} \left( q - \frac{2p\pi}{\lambda} \right) \right] \quad (2)$$

where  $p$  is diffraction order ( $p=1,2$  in our measurements),  $J_p$  is a Bessel function of the first kind,  $\lambda$  is the wrinkling periodicity, the refractive index  $n \approx 1.42$  for PDMS, and the laser wavelength is  $\Lambda=532 \text{ nm}$  with half-width of the aperture  $W \approx 0.5 \text{ mm}$  (SI section S10.1). We introduce a simple ‘sorption-wrinkling model’ to relate the sorption of water with the amplitude of the wrinkles. Eq. 1 governs the normalised mass uptake with time for a specific  $D_{\text{eff}}$ , and we empirically relate the normalised strain with the normalised mass uptake as  $\varepsilon_t/\varepsilon_{\infty} = [(M_t/M_{\infty} - \phi)/(1 - \phi)]^{1/2}$ , where  $\phi \approx 0.08$  is the threshold value below which the film does not swell, thus  $\varepsilon = 0$ , and at time,  $t \rightarrow \infty$ ,  $\varepsilon/\varepsilon_{\infty} = M_t/M_{\infty} = 1$  (SI section S10.2). The wrinkling amplitude, for the bilayer system at small deformations obtained from a linear stability analysis, is related to strain as  $A = h(\varepsilon/\varepsilon_c - 1)^{1/2}$ , where  $\varepsilon_c = 1/4(3\bar{E}_s/\bar{E}_f)^{2/3}$  is the critical strain that must be exceeded to excite the surface instability,  $\bar{E}_f$  and  $\bar{E}_s$  are the plane strain modulus of the oxidised glassy skin and substrate film.<sup>38</sup> For oxidised PDMS bilayers, the plane strain modulus follows  $\bar{E} \equiv E/((1 - \nu^2))$ , where  $E$  is Young’s modulus and  $\nu$  the Poisson ratio ( $E_f \approx 25 \text{ GPa}$ ,  $E_s \approx 1.5 \text{ MPa}$ ,  $\nu_f=0.3$  and  $\nu_s=0.5$ ), while  $h \approx 20 \text{ nm}$  (at  $P=99 \text{ W}$ ,  $t_p=5 \text{ min}$ ,  $p=0.2 \text{ mbar}$ ).<sup>16,17</sup>  $D_{\text{eff}}$  and  $\varepsilon_{\infty}$  were estimated as a function of RH (Fig. 3d), at fixed  $\phi = 0.085$ , to fit the sorption wrinkling model to the SALS inferred wrinkling amplitude values. Figure 3e shows a good agreement between experimentally observed amplitude values and those predicted by the theoretical model, correctly describing the onset of wrinkling. Further model improvements can be introduced by explicitly considering diffusion across the bilayer structure. We utilise the strain values to further simulate the wrinkle profile employing von Kármán elastic nonlinear plate theory following the methodology described in supplementary information (SI section S11). Isotropic wrinkles emerged for a film bonded to a flexible substrate, subjected to equal membrane strains,  $\varepsilon_{11}^0 = \varepsilon_{22}^0 = \varepsilon_{\infty}$  (Fig. 3f).

While the wrinkling wavelength remains largely constant with RH, it is known<sup>20,39</sup> to depend on film thickness  $H$ , as shown in Fig. 3g. PDMS films of varying thickness ( $H$ ) were oxidised under identical conditions (5 min at 99 W), ensuring the formation of a consistent oxide layer with thickness  $h$  across all samples. After oxidation, the films were exposed to air at  $\approx 50\%$  RH, and AFM scans were performed after 24 hours. Sufficiently thin PDMS films do not wrinkle ( $< 200 \text{ nm}$ ) and thick films exhibit extensive cracks ( $> 200 \text{ }\mu\text{m}$ ), competing with wrinkling and eventually covering the entire film surface (SI section S12-13). Following Cerda

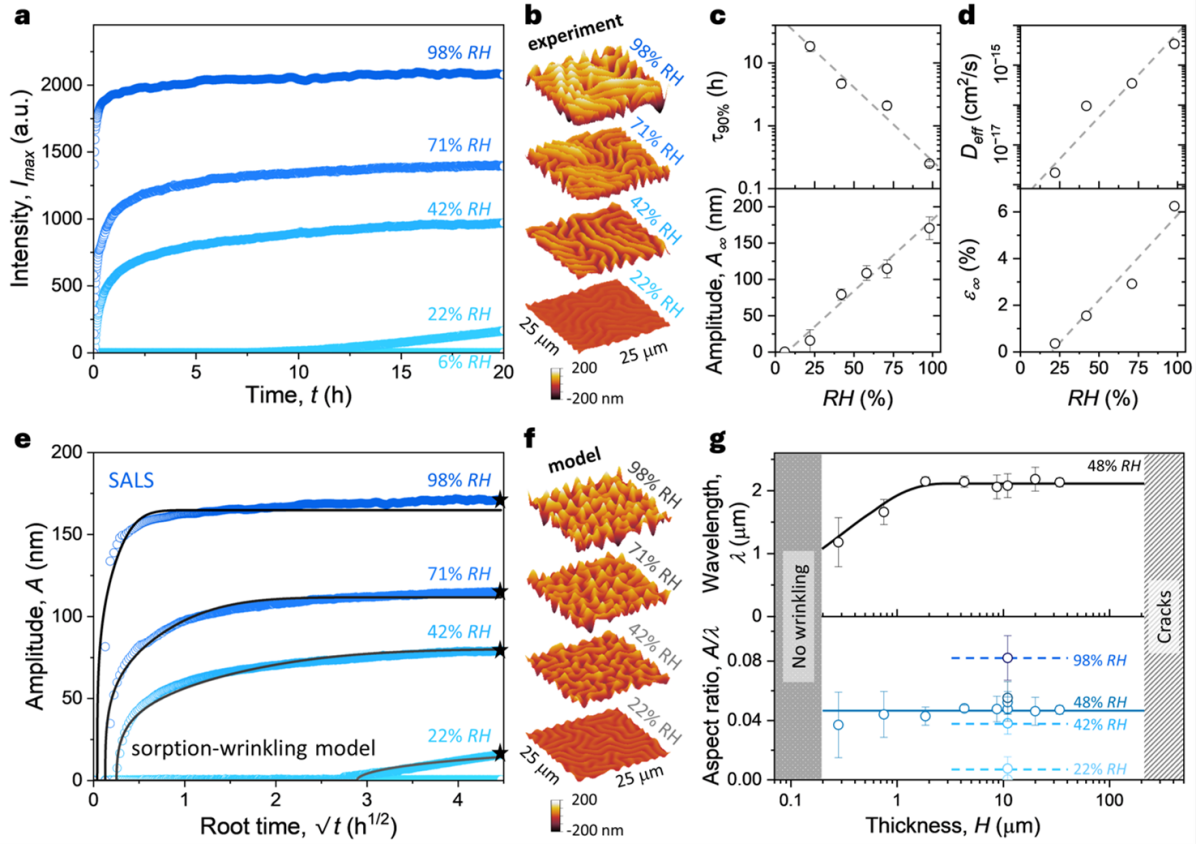


**Figure 3** Water sorption controls wrinkling kinetics. **a**, Evolution of 1<sup>st</sup> order diffraction intensity for plasma oxidised PDMS surfaces (99 W, 5 min, 0.2 mbar,  $H=11 \mu\text{m}$ ) at selected RH. **b**, Corresponding AFM scans at the end of SALS measurement ( $t \simeq 20\text{h}$ ). **c**, Estimated time to 90% of the asymptotic peak SALS intensity,  $\tau_{90\%}$ , and AFM-measured wrinkling amplitude at  $t \rightarrow \infty$ , as a function of RH. **d**, Effective diffusion coefficient,  $D_{\text{eff}}$ , and equilibrium strain values,  $\varepsilon_{\infty}$ , at different RH, employed in the sorption-wrinkling model (see text); dashed lines are guides to the eye. **e**, Wrinkling amplitude computed from SALS ( $\circ$ ) and AFM ( $\star$ ), along with sorption-wrinkling model results (solid lines) using diffusion and strain relations. **f**, Simulated wrinkling profile for films subjected to isotropic membrane strains,  $\varepsilon_{11}^0 = \varepsilon_{22}^0 = \varepsilon_{\infty}$  at the corresponding experimental conditions (see text). **g**, Wrinkling wavelength,  $\lambda$ , and aspect ratio  $A/\lambda$  as a function of PDMS film thickness,  $H$ , for plasma oxidised samples (99 W, 5 min, 0.2 mbar) placed in air (48% RH) for 24 h. Solid line shows the predicted behaviour for wrinkling of a bilayer with finite (eq. 3) and dashed for the  $H \gg h$  limit (see text).

and Mahadevan,<sup>6</sup> and Huang *et al.*,<sup>40</sup> the pattern wavelength and amplitude for a thin, elastic and incompressible substrate of thickness  $H$  are well described by,

$$\lambda = 2\pi h \sqrt{\frac{H}{h} \left( \frac{\bar{E}_f}{18\bar{E}_s} \right)^{\frac{1}{6}}} \quad (3)$$

$$A = h \sqrt{\frac{1}{2} \left( \frac{|N_{11}^0|}{N_c} - 1 \right)}. \quad (4)$$

where  $N_{11}^0$  represents the initial membrane force,  $N_c$  denotes the critical membrane force required for wrinkling to initiate and the membrane force is related to the strain as:  $N/(h\bar{E}_f) = \varepsilon$ . In the limiting case of a thick substrate, the wrinkling equations become independent of substrate thickness and follow the relations  $\lambda = 2\pi h (\bar{E}_f/(3\bar{E}_s))^{1/3}$  and  $A = h(\varepsilon/\varepsilon_c - 1)^{1/2}$ . The aspect ratio of the wrinkles,  $(A/\lambda) = \sqrt{\varepsilon - \varepsilon_c}/\pi$ , is only a function of the strain and independent of the oxidised film and substrate thicknesses (SI section S12). The model, shown by the solid line in Fig. 3g for  $\lambda$  and  $A/\lambda$  as functions of  $H$ , describes all experimental data within measurement uncertainty.

#### 2.4 Reversible sorption and equilibrium wrinkling

We investigate the reversibility of water sorption in oxidised PDMS bilayer films by cycling RH at constant room temperature (21 °C), as well as by cycling temperature at fixed 40% RH (at room temperature), shown in Fig. 4. Employing SALS and the environmental shuttle, a PDMS bilayer was subjected to an RH jump (within  $\leq 20$  min) by forcing humid air, generated with an ultrasonic humidifier, and eventually replaced with a flow of dry air to reduce RH (Fig. 4a). The SALS intensity of the first diffraction order increases with rising RH, reaching equilibrium within  $\approx 5$  h, relaxing slowly towards planarity upon exposure to dry air. The kinetics of the wrinkling pattern formation and relaxation are thus strongly asymmetric. Moreover, at room temperature, while surface wrinkling could evidently be switched ‘on’ or ‘off’ by changes in RH from  $\approx 95\%$  to  $5\%$ , the diffraction intensity did not completely vanish, even after several hours of drying, indicating the presence of residual bound moisture within the film; this differs from freely sorbed water, as it remains persistently associated with the polymer matrix due to molecular interactions, and resistant to drying by exposure to dry air.<sup>41</sup>

While thermal excursion alone is evidently not responsible for

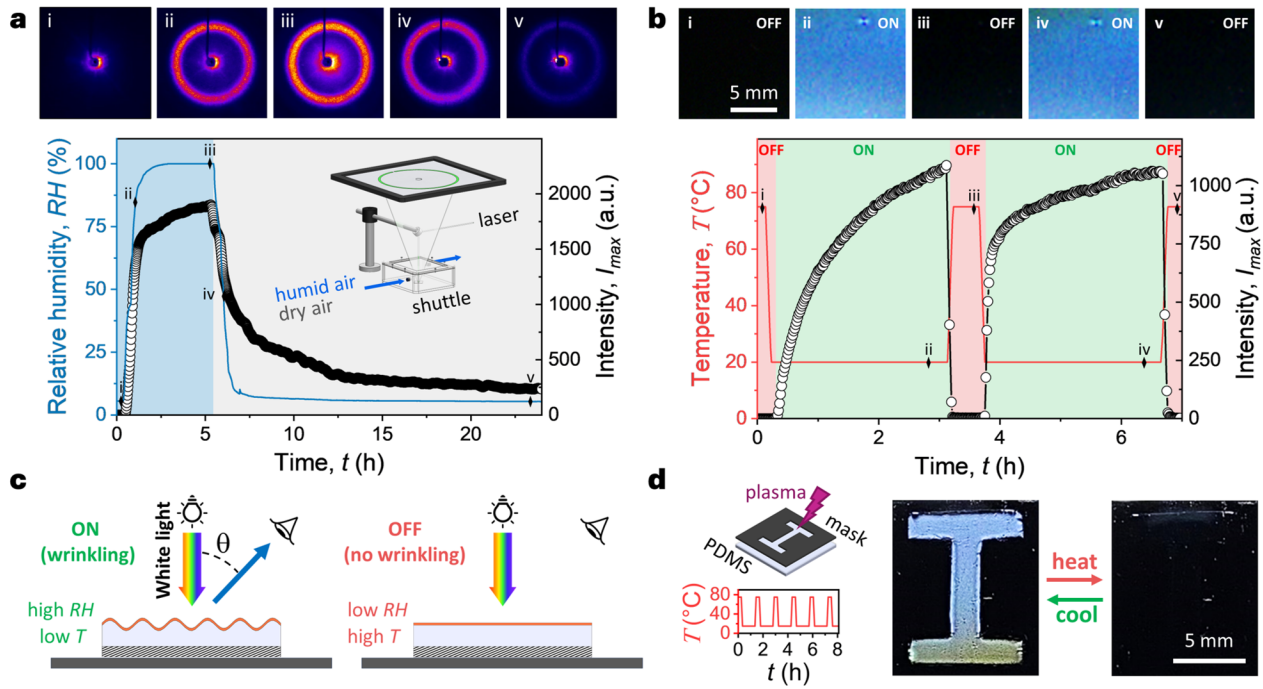


**Figure 4** Dynamic wrinkling for environmental optical sensing. **a**, Plasma-oxidised PDMS ( $H = 11 \mu\text{m}$ ,  $P = 99 \text{ W}$ ,  $t_p = 5 \text{ min}$ ) exposed to dry-humid-dry air cycling at  $21^\circ\text{C}$  during SALS measurements. SALS 2D patterns (i–v) correspond to the markers along the traces shown for RH and intensity of 1<sup>st</sup> diffraction order,  $I_{\text{max}}$ . **b**, Temperature cycling ( $75\text{--}20^\circ\text{C}$ , red solid line) of a PDMS oxidised film in air (40% RH) and resulting  $I_{\text{max}}$  (black circles) and corresponding switching between wrinkling (‘on’ state, green) and planar (‘off’, black); top row: optical images (i–v) of the observed diffractive colour of the surface at angle  $\theta \approx 25^\circ$ , upon white light illumination normal to the surface. **c**, Schematic of plasma-oxidised PDMS surface at low  $T$  and/or high RH, exhibiting wrinkle formation and light diffraction, and reversible transition at low RH and/or high  $T$ . **d**, Plasma-oxidised PDMS surface through a mask, exposed to multiple temperature cycles, yielding a spatially patterned, reversible, optical environmental sensor.

the wrinkling of oxidised PDMS, temperature changes might be expected to play a role, at least indirectly via changing RH. During plasma exposure, the surface temperature of PDMS increases, albeit modestly ( $\Delta T \approx 5\text{--}30^\circ\text{C}$ , depending on plasma pressure, power and duration);<sup>42</sup> at the specific conditions investigated, the temperature rise is  $\Delta T \approx 20^\circ\text{C}$  following plasma exposure (measured by a wireless Arduino-based temperature sensor). Following exposure, the temperature drops along a Newtonian cooling profile (SI section S14). For completeness we thermally equilibrated the PDMS films at defined temperatures (from  $5\text{--}75^\circ\text{C}$ ) prior to plasma exposure, and find that the resulting wrinkling  $\lambda$  and  $A$  remain constant, at fixed RH. However, the onset time of wrinkling, and the kinetics of amplitude growth appear earlier and faster, respectively, upon decreasing temperature. The fact that the asymptotic surface topography remains unchanged with varying temperature profile during surface oxidation, supports our interpretation of equilibrium sorption at fixed RH.

Thermal cycling of oxidised PDMS bilayer films, however, is found to be a powerful yet facile route to switching surface wrinkling ‘on’ or ‘off’, illustrated in Fig. 4b for cycling between  $20^\circ\text{C}$  (at 40% RH, or  $6\text{g/kg}$  absolute humidity) and  $75^\circ\text{C}$  (corresponding to  $\text{RH} \approx 3\%$  for the same absolute humidity), employing a thermal sample stage within the SALS apparatus. The imposed temperature profile is shown by the red line, and the peak diffraction intensity is shown by the black markers. Wrinkles emerge at the lower temperature (higher RH) over a period of hours, switching off rapidly (a ‘reset’) within  $<4 \text{ min}$ , upon heating. The

asymmetry of the profile is attributed to the accelerated moisture release upon heating, where higher temperatures enhance both surface evaporation and internal moisture migration, particularly significant in films with significant internal moisture content, thus enabling fast wrinkle relaxation.

## 2.5 Environmental sensing by sorption-wrinkling-induced diffractive structural colour

In addition to wrinkling of oxidised PDMS induced by organic solvents, tunable wrinkling has also been demonstrated with water vapor by carefully designing bilayer structures where the top layer responds to moisture, including with polyvinyl alcohol (PVA film) on PDMS substrate and UV crosslinking in presence of  $\text{O}_2$ , PVA/laponite (LP) on PDMS/Carbon black substrate, and polystyrene (PS) infused in gelatin on PDMS.<sup>43–45</sup> With these ideas in mind, we demonstrated that our approach can support exceptionally simple and quantitative RH/thermal sensing. Wrinkled PDMS films behave as diffraction gratings,<sup>34–36</sup> we then illuminated the sample normal to the surface ( $0^\circ$ ) with white light, and observed the light intensity at fixed angle  $\theta$  selected such that the diffractive colour for blue is met ( $\theta \approx 25^\circ$ , from  $p\lambda = \lambda \sin(\theta)$ , for the second diffraction order  $p=2$  and wrinkling  $\lambda \approx 2.1 \mu\text{m}$ ), as shown in Fig. 4c. The surface is colourless when ‘off’ and a vibrant blue when wrinkling is ‘turned on’, providing a response to environmental humidity and sample temperature. At high RH or low temperature, wrinkles form due to water sorptions, while

lowering the RH or high temperature returns the planarity of the surface by releasing moisture. Light diffraction, and associated structured colour, of the wrinkled surfaces vary with angle, providing a simple yet robust optical-based temperature and humidity sensor. Moreover, selective plasma exposure of PDMS can be achieved by masking parts of the surface, allowing only designated regions to oxidise. As a result, wrinkling is spatially patterned, enabling these regions to function as localised sensors. Fig. 4d illustrates such a mask, in the shape of the letter 'T', employed during plasma exposure of the PDMS film. After oxidation, the film was subjected to multiple temperature cycles (between 20 °C and 75 °C) while illuminated with white light and observed with an optical camera (SI section S15). The transition between the 'on' and 'off' states was fully reversible, with the sample reliably switching 'on' during cooling and 'off' during heating for multiple consecutive cycles (SI video S1).

### 3 Conclusion

Our work demonstrates that plasma oxidation of PDMS films, which results in the formation of a silica-like skin, involves relatively modest "temperature excursions" that are not responsible for surface wrinkling. Instead, wrinkling takes place due to the differential water sorption between bulk PDMS and the oxidised skin layer, which creates an in-plane stress which, in planar geometries, leads to isotropic patterning. While PDMS wrinkling has been extensively investigated over the past decade, and deployed to develop a range of functional materials and applications, the surface oxidation process has been associated to reproducibility challenges, often attributed to lab-to-lab, instrument and even user variability, or the effect is simply ignored. Our findings show that RH can quantitatively tune wrinkling amplitude, and that this process is dynamic, and reversible. Changes in RH elicit a wrinkling response, within min to h timescales depending on the environmental change, towards an equilibrium value. Significantly, given the temperature dependence of RH, temperature can also be used to modulate and switch wrinkling on/off; for instance, heating at 75 °C can reset a wrinkled surface to planarity within a few minutes. The asymmetry of timescales of wrinkle growth (slow) and decay (fast) with temperature is rationalised in terms of the compounded surface evaporation and internal moisture migration. Equipped with this knowledge, we demonstrate the formation of a new class of inexpensive optical-based thermal and humidity sensor. However, we expect that the ramifications of our work will impact the plethora of current applications of plasma-oxidised PDMS wrinkled, bonded and assembled materials.

### 4 Experimental Section

**PDMS elastomer films.** Polydimethylsiloxane (PDMS) elastomers were prepared by mixing Sylgard 184 (Dow Corning) at 10:1 base to crosslinker ratio, and degassed under vacuum ( $10^{-2}$  mbar) for 20 min; in order to obtain thin films, the mixture was further diluted in hexane ( $\geq 95\%$ , Sigma Aldrich) from 1:0 up to 1:75 PDMS:Hexane ratios, and 0.2 mL of solution spin coated

(Laurell WS 6-400BZ-6NPP Spin Coater) onto silicon squares ([100] single side polished, Inseto UK, 380  $\mu\text{m}$  thick) for 1 min. Wafer pieces 1 cm  $\times$  1 cm were cut with a diamond scribe, cleaned with isopropanol and dried with a compressed air gun prior to use. Film thickness was varied by a combination of spin-coater angular velocities and PDMS:Hexane ratio (e.g., at 6000 rpm, a 1:75 PDMS:Hexane ratio yield  $\approx 100$  nm, while undiluted PDMS produced 11  $\mu\text{m}$  thick films). The films were then thermally crosslinked at 75 °C for 1 h in a convection oven (Binder FD23), and the resulting thickness of the elastomeric films measured with a UV-Vis interferometer (Filmetrics F20-UV) or a digital micrometer (Mitutoyo IP65) as appropriate.

**Plasma oxidation in custom-built glove box.** A custom-made glove box was constructed around a plasma chamber (Diener Femto, 40 kHz) to provide environmental control (gas and humidity). In short, the chamber was designed (Adobe Illustrator) and acrylic sheets (8 mm thick) cut using a CO<sub>2</sub> laser (Universal Laser Systems) and bonded with a polymer sealant & adhesive (C-Tec CT1). Nitrile chemical resistant gloves were attached to the front panel of the glove box via 5-inch duct connector flanges. An access lid was placed on the top panel to allow moving samples in/out of the glove box, and secured tightly using metal toggle clamps. For continuous flow of a specific gas, two pairs of L shape bulkhead union fittings with 6 mm tube push lock were mounted on the sides of the glovebox. A smaller, gas-tight, 'shuttle' box was assembled (based on a Lock & Lock HPL836 rectangular container) to transport the samples for analysis following plasma exposure. To enable light scattering experiments, a section of top panel was removed and replaced with 2 mm borosilicate glass; to maintain a controlled gas environment inside the shuttle, bulkhead union fittings were also attached on the sides. The relative humidity and temperature during the experiments were measured at an interval of 10 s with a wireless digital temperature & RH logger (Lascar electronics, EL-WiFi-TH, accuracy of  $\pm 2\%$  RH and  $\pm 0.3$  °C). The relative humidity inside the shuttle was varied with the help of saturated salt solutions, namely LiCl (11%), MgCl<sub>2</sub> (32%), NaBr (57%), NaCl (75%) and K<sub>2</sub>SO<sub>4</sub> (97%).

Plasma oxidation of the supported PDMS films was carried out using a 40 kHz Diener Femto plasma cylindrical chamber (SI section S1), placed on an aluminium base plate, and operating with oxygen at  $p=0.2$  mbar pressure (corresponding to flow rate  $\approx 5$  sccm). Induction plasma power  $P=99$  W and exposure time  $t_p=5$  min, corresponding to a dose  $D \equiv P \times t_p=29.7$  kJ were fixed in all experiments. After plasma oxidation, the PDMS films were transported for characterization via the shuttle, under controlled environment conditions.

The sample temperature was monitored using a custom built Arduino based wireless temperature sensor, attached to the base plate (comprising a thermistor probe, DS18B20, connected to Arduino-uno powered by 9 V battery) and these temperature values were stored every 10 s in an SD card with the help of a SPI adapter. Temperature control and cycling was imposed using a Linkam stage (THMS600). For selected experiments, the sample temperature prior to plasma treatment was set (5, 45 and 75 °C) or linearly cooled (from 75 °C to 20 °C at 10 °C/min).

**Pattern Characterisation: AFM, SALS, microscopy & structural colour.** Atomic force microscopy (AFM, Bruker Innova) was carried out in tapping mode at 0.5 Hz using Al-coated Si tips (MPP-11100-W, Bruker), and images were analysed with Gwyddion 2.62. Pattern wavelength ( $\lambda$ ) and amplitude ( $A$ ) were averaged from a series of four measurements across  $20 \times 20$  and  $50 \times 50 \mu\text{m}^2$  images.

A custom-built small-angle light scattering (SALS), set up in reflection mode, was employed to examine the environment and time-dependent evolution of the surface diffraction pattern of the isotropic wrinkles of the PDMS films. The SALS setup depicted in Fig. 1b was assembled using a green diode-pumped laser ( $\Lambda=532$  nm, 500 mW, CrystaLaser), diaphragm, spatial filter and neutral density filter wheel (ND 0.2-0.6 and 1.0-4.0), and  $45^\circ$  mirror (all Thorlabs) aligned such that the laser beam impinged normal to the PDMS films supported on silicon. The resulting diffraction patterns were projected on a tracing screen above and captured using a Hamamatsu Orca thermoelectrically cooled detector. Automated time-lapse image acquisition of the diffraction patterns was controlled using the in-built Wasabi software. The wavelength of the wrinkling pattern was obtained from the wavenumber of maximum intensity  $q^*$ , as  $\lambda = 2\pi/q^*$  where  $q = (4\pi/\Lambda) \sin(\theta/2)$  and  $\theta$  is the scattering angle. The intensity profile was background subtracted ( $t = 2$  min) and radially averaged using ImageJ, and analysed in the framework of a tunable surface diffraction grating (see text).

Optical images of PDMS beam bending and structural colour of wrinkled surfaces were recorded using CMOS camera (Basler acA640-750uc) equipped with a fixed focal length lens (Edmund optics 67709). Samples were illuminated from above with a white light source (Advanced Illumination). Optical microscopy images of surface cracks were captured using a reflection microscope (Olympus BX41) equipped with CMOS camera (Basler acA2000-165uc). Diffraction SALS patterns and optical images were processed and analysed with ImageJ.

**Surface analysis: FTIR and XPS spectroscopies.** FTIR spectral analysis was carried out on PDMS films exposed to 4% and 98% relative humidity (RH) post plasma treatment for varying durations, employing a Bruker Ingenio S spectrometer in attenuated total reflectance (ATR) mode with a diamond crystal serving as the internal reflection element (IRE). The films were positioned with the glassy skin in contact with the IRE. A clean, dry diamond crystal (IRE) was consistently used for background correction. Each spectrum was collected with 64 scans over a range of 4000 to 600  $\text{cm}^{-1}$  at a spectral resolution of 4  $\text{cm}^{-1}$ . The data were analysed in absorbance units and processed using OPUS 8.5 software. Spectral subtraction of the dry sample and standard baseline corrections were applied with no additional data processing performed.

X-ray photoelectron spectroscopy was carried out using a Thermo-Scientific K-Alpha ( $h\nu = 1486.6$  eV), employing a binding energy range of 0–1100 eV with a step size of 0.5 eV. Data were analysed with Avantage software.

**Quartz crystal microbalance.** QCM-D (Biolin scientific) with dissipation monitoring was employed to quantify the difference in

water sorption between surface oxidised PDMS and bulk PDMS. PDMS films (PDMS:Hexane 1:75, spincoated at 6000 rpm for 1 min) were placed on Au sensors (QX301 Q-sense) and cured at  $75^\circ\text{C}$  for 1 h. Half of the samples were oxidised in plasma (99 W, 5 min, 0.2 mbar), while the other half were left in the neat state. The glovebox was controlled at low RH ( $\approx 5\%$ ) while oxygen plasma treatment took place, and the oxidised films on the Au sensor were transferred to the QCM module via the shuttle. The relative humidity in the vicinity of the sample during QCM measurement was manipulated with the help of flow module (QHM 401, Q-sense). After placing the sample in the flow module, the module was purged with saturated salt solution exhibiting low RH (LiCl 11%) at a flow rate of  $100 \mu\text{L min}^{-1}$  (Ismatec peristaltic pump, ISM795) for 15 min. Subsequently, high RH saturated salt solution ( $\text{K}_2\text{SO}_4$  97%) was introduced in the flow rate at the same flow rate. Mass uptake was estimated by relating the change in resonant frequency of the coated gold (Au) sensor with the change in mass, following the Sauerbrey equation,<sup>46</sup>

$$\Delta f = -C \frac{\Delta m}{n} \quad (5)$$

where  $\Delta m$  is the change in mass per unit area ( $\text{ng}/\text{cm}^2$ ),  $\Delta f$  is the change in resonance frequency (Hz),  $C$  is the mass sensitivity constant of the quartz crystal ( $18 \text{ ng}/(\text{cm}^2 \text{ Hz})$  for a 5 MHz crystal, which depends on the properties of the crystal used), and  $n$  is the overtone number (harmonic number). Water mass fraction is estimated as:

$$M_w = \frac{\Delta f_i - \Delta f_{film}}{\Delta f_i - \Delta f_{blank}} \times 100 \% \quad (6)$$

where  $M_w$  is the change in water mass fraction,  $\Delta f_{film}$  and  $\Delta f_i$  are the resonance frequency of the QCM sensor coated with the film at 11% RH and at 97% RH at time  $t$  respectively, and  $\Delta f_{blank}$  is the resonance frequency of the QCM sensor without coating.

## Acknowledgements

ZA thanks the Department of Chemical Engineering, Imperial College London for a PhD scholarship. We thank EPSRC and P&G for funding (EP/V056891/1). JTC acknowledges the Royal Academy of Engineering (RAEng, UK) for funding a Research chair, and the Royal Society (IES/R2/222241) for an international exchange grant. PP and PICT acknowledge funding from the Portuguese Foundation for Science and Technology (FCT), Portugal. We thank Advanced Hackspace Imperial College London, for access to prototyping facilities ( $\text{CO}_2$  Laser and micro-controllers). We thank Serafim Kalliadasis for useful discussions on diffusion modeling, and Martin Trusler for advice on humidity sensing.

## Author Contributions

ZA and JTC designed the project and planned the work. ZA built the environmental chamber and shuttle, customised the SALS setup (with JTC), carried out experiments, aided by SX (QCM) and GT (XPS, FTIR). SX and JH helped with QCM data interpretation. PP and PT coded the wrinkling model. CS and JFD helped with the skin and wrinkling data interpretation. ZA and JTC wrote the first draft and all authors revised the paper.

## References

- 1 Y. Xia and G. M. Whitesides, *Angewandte Chemie International Edition*, 1998, **37**, 550–575.
- 2 J. Genzer and J. Groenewold, *Soft Matter*, 2006, **2**, 310–323.
- 3 H. Allen, *Analysis and Design of Structural Sandwich Panels*, Pergamon, 1969.
- 4 A. Volynskii, S. Bazhenov, O. Lebedeva and N. Bakeev, *Journal of Materials Science*, 2000, **35**, 547–554.
- 5 R. Huang, *Journal of the Mechanics and Physics of Solids*, 2005, **53**, 63–89.
- 6 E. Cerda and L. Mahadevan, *Physical Review Letters*, 2003, **90**, 074302.
- 7 S. Yang, K. Khare and P.-C. Lin, *Advanced Functional Materials*, 2010, **20**, 2550–2564.
- 8 N. Bowden, S. Brittain, A. G. Evans, J. W. Hutchinson and G. M. Whitesides, *Nature*, 1998, **393**, 146–149.
- 9 Y.-C. Chen and A. J. Crosby, *Advanced Materials (Deerfield Beach, Fla.)*, 2014, **26**, 5626–5631.
- 10 J. Rodriguez-Hernandez, *Progress in Polymer Science*, 2015, **42**, 1–41.
- 11 J. C. McDonald, D. C. Duffy, J. R. Anderson, D. T. Chiu, H. Wu, O. J. Schueller and G. M. Whitesides, *Electrophoresis*, 2000, **21**, 27–40.
- 12 J. C. McDonald and G. M. Whitesides, *Accounts of Chemical Research*, 2002, **35**, 491–499.
- 13 H. Hillborg and U. Gedde, *Polymer*, 1998, **39**, 1991–1998.
- 14 M. Ouyang, C. Yuan, R. Muisener, A. Boulares and J. Koberstein, *Chemistry of Materials*, 2000, **12**, 1591–1596.
- 15 K. Efimenko, W. E. Wallace and J. Genzer, *J. Colloid Interface Sci.*, 2002, **254**, 306 – 315.
- 16 F. A. Bayley, J. L. Liao, P. N. Stavrinou, A. Chiche and J. T. Cabral, *Soft Matter*, 2014, **10**, 1155–1166.
- 17 M. Nania, O. K. Matar and J. T. Cabral, *Soft Matter*, 2015, **11**, 3067–3075.
- 18 N. Bowden, W. T. Huck, K. E. Paul and G. M. Whitesides, *Applied Physics Letters*, 1999, **75**, 2557–2559.
- 19 A. Tserepi, E. Gogolides, K. Tsougeni, V. Constantoudis and E. S. Valamontes, *Journal of Applied Physics*, 2005, **98**, 113502.
- 20 H. Evensen, H. Jiang, K. Gotrik, F. Denes and R. Carpick, *Nano letters*, 2009, **9**, 2884–2890.
- 21 D. B. Chua, H. Ng and S. F. Li, *Applied Physics Letters*, 2000, **76**, 721–723.
- 22 D. Breid and A. J. Crosby, *Soft Matter*, 2011, **7**, 4490–4496.
- 23 S. M. Wiederhorn, F. Yi, D. LaVan, L. J. Richter, T. Fett and M. J. Hoffmann, *Journal of the American ceramic society*, 2015, **98**, 78–87.
- 24 N. K. Nadermann, E. P. Chan and C. M. Stafford, *ACS Applied Materials & Interfaces*, 2015, **7**, 3492–3502.
- 25 M. Nania, F. Foglia, O. K. Matar and J. T. Cabral, *Nanoscale*, 2017, **9**, 2030–2037.
- 26 A. Nistor, G. Stiubianu, C. Racles and M. Cazacu, *Mater. Plast*, 2011, **48**, 33–37.
- 27 J. Crank, *The mathematics of diffusion*, Oxford university press, 1979.
- 28 B. D. Vogt, C. L. Soles, H.-J. Lee, E. K. Lin and W.-I. Wu, *Polymer*, 2005, **46**, 1635–1642.
- 29 D. A. Markov, E. M. Lillie, S. P. Garbett and L. J. McCawley, *Biomedical microdevices*, 2014, **16**, 91–96.
- 30 A. Zouine, O. Dersch, G. Walter and F. Rauch, *Physics and Chemistry of Glasses-European Journal of Glass Science and Technology Part B*, 2007, **48**, 85–91.
- 31 N. L. Thomas and A. Windle, *Polymer*, 1982, **23**, 529–542.
- 32 H. S. Kim and A. J. Crosby, *Advanced materials*, 2011, **36**, 4188–4192.
- 33 S. Cai, D. Breid, A. J. Crosby, Z. Suo and J. W. Hutchinson, *Journal of the Mechanics and Physics of Solids*, 2011, **59**, 1094–1114.
- 34 C. Harrison, C. M. Stafford, W. Zhang and A. Karim, *Applied Physics Letters*, 2004, **85**, 4016–4018.
- 35 A. Tan, L. Pellegrino and J. T. Cabral, *ACS Applied Polymer Materials*, 2021, **3**, 5162–5170.
- 36 A. Tan, L. Pellegrino, Z. Ahmad and J. T. Cabral, *Advanced Optical Materials*, 2022, **10**, 2200964.
- 37 K. Wu, T. Zhu, L. Zhu, Y. Sun, K. Chen, J. Chen, H. Yuan, Y. Wang, J. Zhang, G. Liu *et al.*, *Nano Letters*, 2022, **22**, 2261–2269.
- 38 A. Chiche, C. M. Stafford and J. T. Cabral, *Soft Matter*, 2008, **4**, 2360.
- 39 D. C. Hyun and U. Jeong, *Journal of Applied Polymer Science*, 2009, **112**, 2683–2690.
- 40 Z. Huang, W. Hong and Z. Suo, *Journal of the Mechanics and Physics of Solids*, 2005, **53**, 2101–2118.
- 41 A. S. Mujumdar, *Handbook of industrial drying*, CRC press, 2006.
- 42 Z. Ahmad, B. Parias M. R, H. Barr and J. T. Cabral, *Nano Letters*, 2024, **25**, 740–746.
- 43 S. Zeng, R. Li, S. G. Freire, V. M. Garbellotto, E. Y. Huang, A. T. Smith, C. Hu, W. R. Tait, Z. Bian, G. Zheng *et al.*, *Advanced Materials*, 2017, **29**, 1700828.
- 44 S. Zeng, Y. Liu, S. Li, K. Shen, Z. Hou, A. P. Chooi, A. T. Smith, Z. Chen and L. Sun, *Advanced Functional Materials*, 2021, **31**, 2009481.
- 45 S. Zhu, Y. Liu, W. Guo, J. Fan, X. Jiang and J. Li, *Advanced Functional Materials*, 2023, **33**, 2301850.
- 46 I. Reviakine, D. Johannsmann and R. P. Richter, *Analytical Chemistry*, 2011, **83**, 8838–8848.